Supporting Information

Oliver et al. 10.1073/pnas.1208699109

SI Text

1. Stability and Cleanliness of W Tip. He gas for field ion microscopy (FIM) is leaked into the chamber through the wall of a custom-blown glass tube. The tube is heated to ∼200 °C to increase the permeability of the glass wall to He; because of the small molecular size of He, this use of He is exceptionally selective, with He having at least 10^5 greater permeability than any other gas. The main source of contaminants during FIM is the necessity to close off the turbo pump for the duration: a resting pressure of $\sim 10^{-9}$ mbar (in the absence of He) is generally obtained.

We have routinely imaged tips both before and after performing indentations. An example is shown in Fig. S2. Some desorbents are typically observed during voltage ramping when FIM is performed after indentation, likely including gold transferred to the tip during measurements. After a stable imaging voltage is attained, a tungsten tip with the same size and structure as before indenting is generally observed.

In some cases, however, an instability or tip crash occurs, which alters the tungsten tip. This crash may be apparent in the FIM as a dislocation or crack, which is visible in Fig. S3, or grosser alterations to the tip shape may render it too blunt to be imaged. The latter was the case with the tip used to obtain the results in the paper. We note, however, that, when such a tip-destructive event occurs, it is generally clearly evident in the force signal, which was acquired continuously in our experiment whenever the tip was in proximity to the surface. The tip crash that damaged this tip occurred after all of the measurements reported here were collected.

To confirm that gross alterations to the tungsten tip structure under normal indentation conditions are unlikely, we consider the stresses in the tungsten tip. The elastic analyses used to deduce the contact area (described in *Methods*) also describe the stress state in both the indenter and sample. At the observed yield load of 200 nN, the Derjaguin–Muller–Toporov model predicts a principle shear stress of 5.4 GPa, and the Hertzian model predicts a somewhat higher value of 6.3 GPa. The ideal shear strength of a perfect crystal can be derived approximately as $\hat{o}_\chi = \Gamma/2\delta$, where G is the shear modulus (1). For gold, G = 27 GPa; therefore, $\hat{o}_\chi = 4.3$ GPa, which is comparable with the predicted yield stress. For tungsten, G = 161 GPa, and $\hat{o}_\chi = 25.6$ GPa. Thus, under normal loading conditions, we expect plasticity to be confined to the gold substrate. This result was supported by the molecular dynamics simulations that we carried out, in which plastic defects were observed exclusively in the gold substrate.

2. Correction to Measured Junction Conductance for Wire Resistance. To accurately determine the conductance through the nanomechanical junction, the measured total resistance should be corrected for the contribution of the macroscopic W wire. The electrochemically etched wire is effectively conical close to the tip, flaring out as it approaches the unetched wire shank (2). To determine resistance, the wire can be modeled as a semiinfinite truncated cone. The cone's base is defined as the edge of the ballistic transport region, taken to be a distance from the junction equal to the mean free path of electrons in tungsten (∼20 nm) (3). The resistance of a semiinfinite truncated cone is (Eq. **S1**)

$$R = \frac{\rho}{\pi \tan(\alpha/2) r}, \qquad \textbf{[S1]}$$

where R is resistance, ρ is resistivity, α is the cone angle, and r is the base radius. This calculation gives a resistance in our case of $R \sim 35\ \Omega$.

3. Onset of Irreversible Plastic Deformation. Fig. S4 shows that irreversible plastic deformation, identifiable as a significant hysteresis energy in the force–displacement curve, begins at ∼200 nN for the 4.1 nm W tip used in this study. The low positive values of hysteresis energy below this force are caused by adhesion on retraction of the tip from the surface.

4. Calculation of Hysteresis Energy from Force–Displacement Curves. Hysteresis energy was calculated as the area between the loading and unloading force–displacement curves (Fig. S5) or more precisely, the area under the loading curve minus the area under the unloading curve, equivalent to the net work done by the indenter and equivalent to the energy dissipated in the material by irreversible processes. This energy is positive for all dissipative processes, such as subsurface plasticity, surface rearrangements, and adhesion-induced necking.

5. Evolution of Conductance over Repeated Indentation Cycles. The data were further analyzed to investigate the evolution of conductance over repeated indentation cycles. The results are shown in Fig. S6. Each data point represents a sequence of indentations. On the x axis is plotted the ratio of the maximum conductance for the first indentation in the sequence to the theoretical upper bound for that maximum load [corresponding to the plastic upper bound (dashed dotted lines) in Fig. 3*A* for loads > 200 nN and the Johnson–Kendall–Roberts upper bound (dashed line) for loads < 200 nN]. The y axis is the ratio of the maximum conductance of the 5th or 10th indentation in the sequence to the maximum conductance of the first indentation. Thus, the x axis value indicates how high the conductance is in relative terms at the beginning of a sequence; the y axis indicates the direction and magnitude of evolution of conductance during the sequence. It is apparent that, where the initial conductance is close to the upper bound, the nth cycle/first cycle ratio is less than zero, indicating an evolution to lower conductance. Conversely, where the initial conductance is very low, the ratio indicates an evolution to higher conductance. This behavior is intuitively reasonable. The equilibrium value seems to be somewhere between 10^{-2} and 10^{-1} of the theoretical upper bound. This finding may correspond to a most likely or most stable defect configuration in the Au beneath the W tip.

Fig. S7 shows that this evolution of conductance to an equilibrium value is observed both for indents below the plastic threshold and indents above. This finding suggests that the phenomenon involves rearrangement of the atoms at the tungsten–gold interface, including any contaminants at the interface, as well as or instead of the evolution of subsurface defects.

6. Ballistic and Diffusive Contributions to Conductance in the Presence of Vacancies. In Fig. S8, we present the conductance of Au in the case of random vacancies. One finds that, for 30% vacancies, the conductance drops by 4× compared with a perfect lattice of Au atoms. In addition, the total conductance is decomposed into ballistic and diffusive contributions, where the former corresponds to electrons traversing the imperfect material without scattering and the latter indicates the contribution from carriers having scattered one time or more off the vacancies. The ballistic conductance decreases rapidly with vacancies; however, the total conductance remains relatively high because of the diffusive conductance. The diffusive contribution is found to initially increase with vacancy concentration, because the probability of a carrier scattering off a vacancy increases with the number of vacancies. After ∼10%, the diffusive conductance decreases, because the conduction pathway for carriers becomes inhibited.

1. Hull D, Bacon DJ (1984) *Introduction to Dislocations* (Pergamon, Oxford), 3rd Ed.
2. Hagedorn T, et al. (2011) Refined tip preparation by electrochemical etching and ultrahigh vacuum treatment to obtain atomically sharp tips for scanning tunneling microscope and atomic force microscope. *Rev Sci Instrum* 82(11):113903–113905.
3. Choi D, et al. (2012) Electron mean free path of tungsten and the electrical resistivity of epitaxial (110) tungsten films. *Phys Rev B* 86:045432.

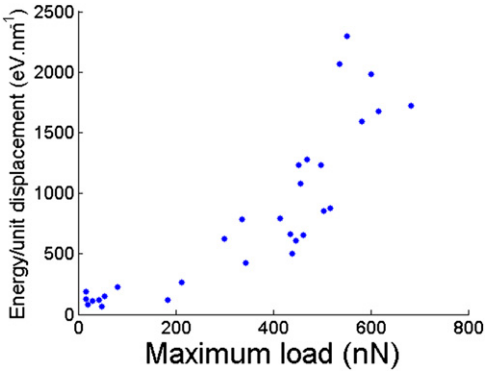

Fig. S1. Hysteresis energy per unit displacement vs. maximum load for initial curves.

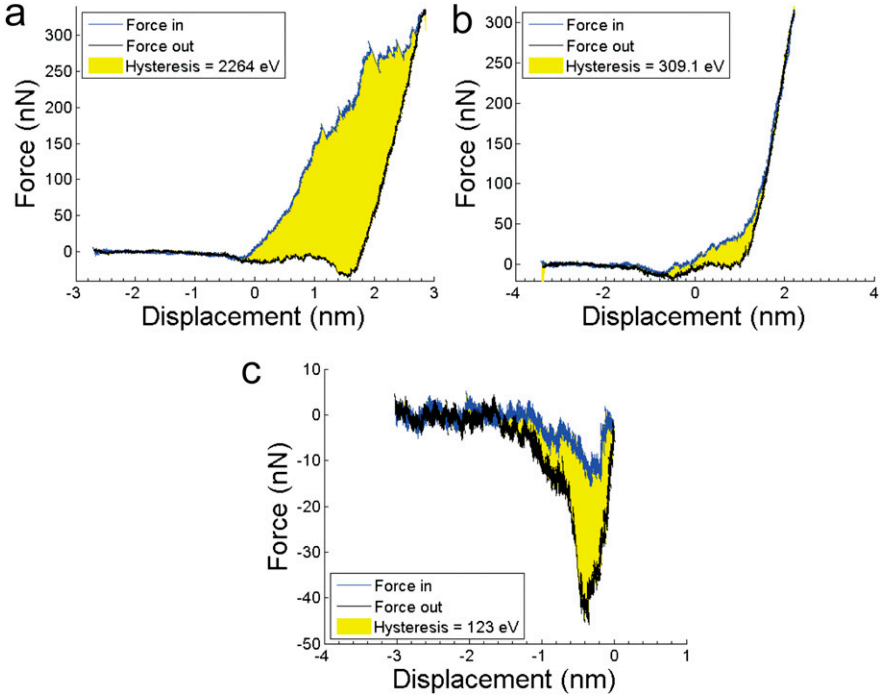

Fig. S2. Force–displacement plots showing hysteresis energy (the area between loading and unloading curves; shaded yellow). (*A*) Initial indent in a sequence showing large hysteresis from plasticity. (*B*) Third indent in the same sequence showing smaller hysteresis at low loads that is attributable to surface rearrangements and adhesion. (*C*) An approach below the onset of net repulsive force showing hysteresis caused by surface dissipative processes.

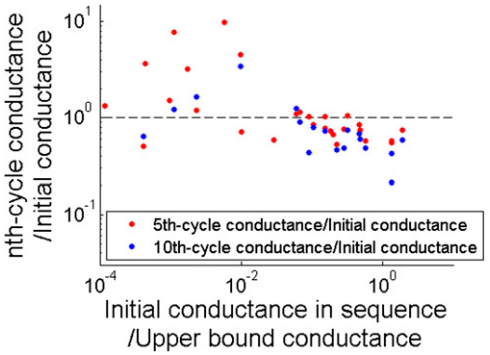

Fig. S3. The ratio of first-indent conductance over upper-bound conductance vs. the ratio of nth-indent conductance over first-indent conductance. When the initial conductance in a sequence is relatively high, the conductance subsequently decreases, and vice versa.

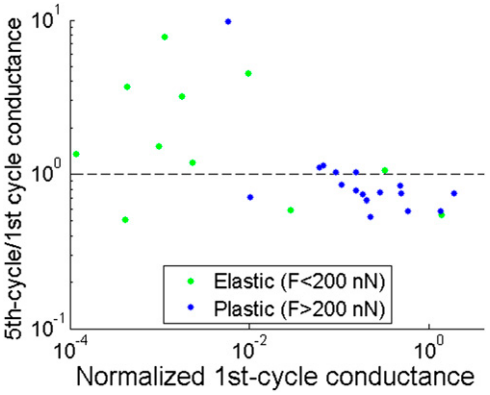

Fig. S4. The ratio of first-indent conductance over upper-bound conductance vs. the ratio of 10th-indent conductance over first-indent conductance; indents below the plastic threshold are colored in green, and indents above the plastic threshold are colored in blue.

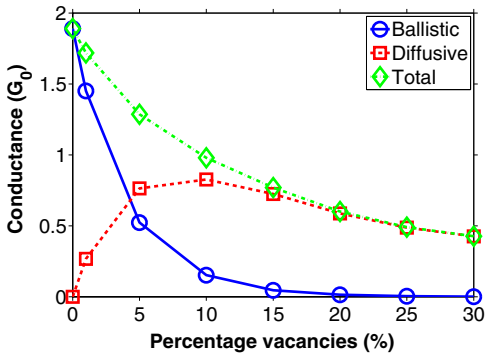

Fig. S5. Conductance vs. percentage vacancies in Au. The total conductance is separated into two contributions, namely ballistic and diffusive. Note that the conductance values correspond to a cross-sectional area of 0.406 × 0.406 nm.

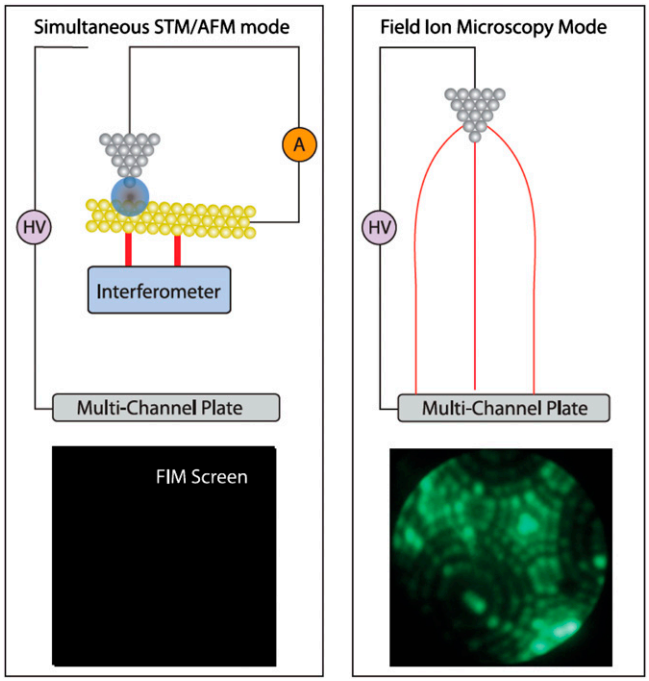

Fig. S6. The key features of the experimental system used in this study are illustrated schematically (1). All measurements are prepared in a dedicated ultra-high vacuum chamber. In scanning probe/indentation mode, the flexible sample allows forces to be detected using optical inteferometry; current between the sample and tip is measured simultaneously. In FIM mode, the sample is moved to one side, exposing the multichannel plate (MCP) detector; He is leaked in, and a high voltage is applied between the tip and MCP to obtain an FIM image.

1. El Ouali M (2010) Nanometre scale indentation: Effect of very sharp indenters on adhesion, plasticity, and electronic transport. PhD thesis (McGill University, Montreal).

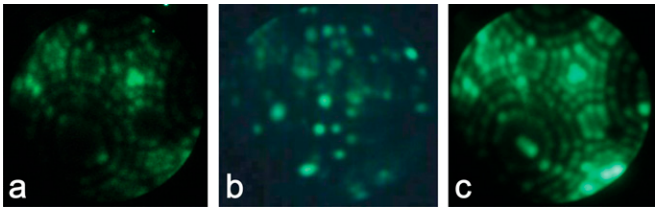

Fig. S7. FIM images of a W tip taken (*A*) immediately before nanoindentation, (*B*) immediately after acquisition of a few hundred load–displacement curves, and (*C*) after field evaporation of adsorbates, showing recovery of the original tip structure.

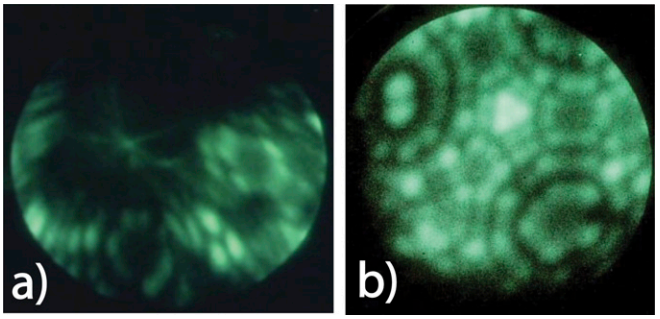

Fig. S8. (*A*) FIM image of a W tip damaged after a catastrophic tip crash. (*B*) FIM image of an undamaged tip for comparison, showing uninterrupted threefold symmetry and an absence of image distortion.

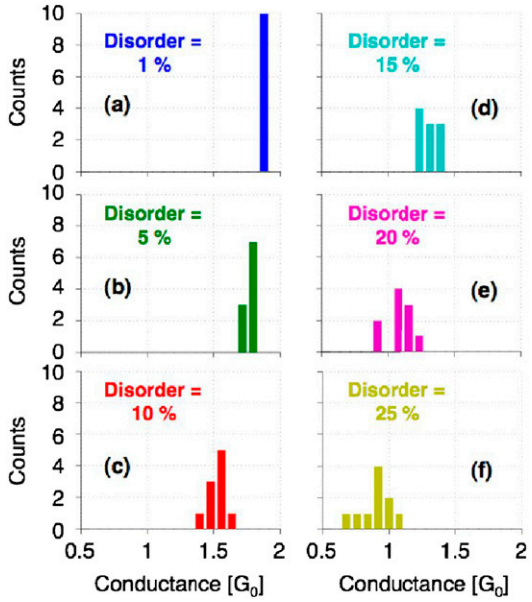

Fig. S9. Conductance histogram for 10 randomly generated Au structures as a function of disorder parameter $d_M = 1\%$ (*A*), 5% (*B*), 10% (*C*), 15% (*D*), 20% (*E*), and 25% (*F*). d_M times the Au–Au bond length (2.87 Å) corresponds to the maximum possible random displacement around the ideal lattice site.